

## The Structure of A $\beta$ 42 C-Terminal Fragments Probed by a Combined Experimental and Theoretical Study

Chun Wu<sup>1†</sup>, Megan M. Murray<sup>1†</sup>, Summer L. Bernstein<sup>1†</sup>,  
Margaret M. Condron<sup>2</sup>, Gal Bitan<sup>2,3</sup>, Joan-Emma Shea<sup>1,4\*</sup>  
and Michael T. Bowers<sup>1\*</sup>

<sup>1</sup>Department of Chemistry and Biochemistry, University of California, Santa Barbara, CA 93106-9501, USA

<sup>2</sup>David Geffen School of Medicine, University of California, Los Angeles, CA 90095, USA

<sup>3</sup>Brain Research Institute and Molecular Biology Institute, University of California, Los Angeles, CA 90095, USA

<sup>4</sup>Department of Physics, University of California, Santa Barbara, CA 93106-9501, USA

Received 26 November 2008;  
received in revised form  
13 January 2009;

accepted 17 January 2009

Available online  
23 January 2009

Edited by D. Case

The C-terminus of amyloid  $\beta$ -protein (A $\beta$ ) 42 plays an important role in this protein's oligomerization and may therefore be a good therapeutic target for the treatment of Alzheimer's disease. Certain C-terminal fragments (CTFs) of A $\beta$ 42 have been shown to disrupt oligomerization and to strongly inhibit A $\beta$ 42-induced neurotoxicity. Here we study the structures of selected CTFs [A $\beta$ ( $x$ -42);  $x$ =29–31, 39] using replica exchange molecular dynamics simulations and ion mobility mass spectrometry. Our simulations in explicit solvent reveal that the CTFs adopt a metastable  $\beta$ -structure:  $\beta$ -hairpin for A $\beta$ ( $x$ -42) ( $x$ =29–31) and extended  $\beta$ -strand for A $\beta$ (39–42). The  $\beta$ -hairpin of A $\beta$ (30–42) is converted into a turn-coil conformation when the last two hydrophobic residues are removed, suggesting that I41 and A42 are critical in stabilizing the  $\beta$ -hairpin in A $\beta$ 42-derived CTFs. The importance of solvent in determining the structure of the CTFs is further highlighted in ion mobility mass spectrometry experiments and solvent-free replica exchange molecular dynamics simulations. A comparison between structures with solvent and structures without solvent reveals that hydrophobic interactions are critical for the formation of  $\beta$ -hairpin. The possible role played by the CTFs in disrupting oligomerization is discussed.

© 2009 Elsevier Ltd. All rights reserved.

**Keywords:** Alzheimer A $\beta$ 42 C-terminal fragments; ion mobility; molecular dynamics simulations;  $\beta$ -hairpin

### Introduction

Oligomerization of amyloid  $\beta$ -protein (A $\beta$ ) is believed to be a critical event in the development of

Alzheimer's disease (AD).<sup>1,2</sup> *In vivo* studies show that A $\beta$  oligomers (A $\beta$  dimers<sup>3</sup> or putative dodecamers<sup>4,5</sup>) are the primary toxins causing AD. A $\beta$  is found primarily as either a 40-amino-acid peptide or a 42-amino-acid peptide, differing only in the addition of two hydrophobic residues (I41 and A42) to the C-terminus of the former. This small difference in primary structure translates into large differences in the oligomerization patterns of A $\beta$ 40 and A $\beta$ 42.<sup>6–10</sup> Both photo-induced cross-linking of unmodified proteins experiments<sup>9</sup> and ion mobility experiments<sup>10</sup> have shown that A $\beta$ 40 and A $\beta$ 42 have distinct oligomer distributions. Monomers of A $\beta$ 40 oligomerize to form dimers, trimers, and tetramers, but A $\beta$ 42 oligomerizes further to form hexamers (paranuclei) and dodecamers.<sup>9,10</sup> Moreover, A $\beta$ 42 oligomers are significantly more neurotoxic than A $\beta$ 40.<sup>11</sup> Mutations in presenilins that are associated with familial AD have been shown to increase the A $\beta$ 42/A $\beta$ 40 ratio *in vivo*.<sup>12</sup>

\*Corresponding authors. J.-E. Shea is to be contacted at Department of Chemistry and Biochemistry, University of California, Santa Barbara, CA 93106-9501, USA. E-mail addresses: [shea@chem.ucsb.edu](mailto:shea@chem.ucsb.edu); [bowers@chem.ucsb.edu](mailto:bowers@chem.ucsb.edu).

† C.W., M.M.M., and S.L.B. contributed equally to this work.

Abbreviations used: A $\beta$ , amyloid  $\beta$ -protein; CTF, C-terminal fragment; AD, Alzheimer's disease; REMD, replica exchange molecular dynamics; IM-MS, ion mobility mass spectrometry; ATD, arrival time distribution; MD, molecular dynamics; nano-ESI, nano-electrospray ionization; MALDI, matrix-assisted laser desorption/ionization.

A $\beta$ 42 fibrillizes faster than A $\beta$ 40—a process that may be driven by the more hydrophobic C-terminus of the A $\beta$ 42.<sup>13</sup> Still, the mechanism by which the C-terminus accelerates the oligomerization of A $\beta$ 42 is not well understood. Whether the C-terminal residues (IA) in A $\beta$ 42 facilitate self-assembly via nonspecific hydrophobic interactions and/or promote the formation of an ordered conformation (e.g.,  $\beta$ -sheet) is still an open question. A possible mechanism is one in which increased hydrophobicity marginally favors not only generic hydrophobic association but also  $\beta$ -structuring (formation of  $\beta$ -strand or  $\beta$ -hairpin) of the C-terminus. This  $\beta$ -structuring may selectively increase the kinetics of ordered oligomerization and fibril formation of full-length A $\beta$ 42 relative to A $\beta$ 40.<sup>7,14–16</sup> Previous studies have provided some evidence. Solution NMR experiments, as well as an *in silico* study, demonstrated that both A $\beta$ 40 and A $\beta$ 42 have similar collapsed-coil configurations with one exception: the C-terminus of A $\beta$ 42 contains a turn that is not apparent in A $\beta$ 40.<sup>6,17–19</sup> Many other studies<sup>15,17,20,21</sup> show that the C-terminus of A $\beta$ 42 is more rigid than that of A $\beta$ 40, suggesting the presence of a quasi-stable conformation in the former. Still, a higher-resolution structural characterization of the C-terminal region is needed in order to determine whether the assembly of A $\beta$ 42 is accelerated relative to A $\beta$ 40 by the formation of  $\beta$ -conformation in the C-terminus.

The apparent importance of the C-terminus in the assembly of A $\beta$ 42 and the particularly strong link of A $\beta$ 42 to AD suggest that the C-terminus of A $\beta$ 42 is a good target for developing inhibitors that disrupt A $\beta$ 42 oligomerization as a means of preventing and treating AD. Recent experiments have shown that C-terminal fragments (CTFs) of A $\beta$ 42 were capable of disrupting the oligomerization and of inhibiting the neurotoxicity of full-length A $\beta$ 42.<sup>22</sup> Among the CTFs [A $\beta$ ( $x$ -42);  $x$ =28–39] tested, three fragments showed particularly strong inhibitory effects: A $\beta$ (31–42), A $\beta$ (30–42), and A $\beta$ (39–42), the shortest CTF tested. In particular, A $\beta$ (31–42), A $\beta$ (30–42), and A $\beta$ (39–42) inhibited 100%, 80%, and 80% of A $\beta$ -induced toxicity, respectively. Although both A $\beta$ (31–42) and A $\beta$ (39–42) formed nontoxic heterooligomers with A $\beta$ 42 monomers, the mechanism was different: A $\beta$ (31–42) was a stronger inhibitor of intermolecular interactions among A $\beta$ 42 monomers, whereas A $\beta$ (39–42) was a stronger inhibitor of intramolecular interactions within A $\beta$ 42 monomers. Further study showed that an A $\beta$ 40-derived CTF, A $\beta$ (30–40), did not affect paranucleus formation, but did inhibit A $\beta$ 42-induced toxicity to the same extent that A $\beta$ (30–42) did (H. Li, B. H. Monien, A. Lomakin, E. A. Fradinger, S. M. Spring, B. Urbanc, G. B. Benedek, G. Bitan, Mechanistic investigation of C-terminal fragments as inhibitors of A $\beta$ 42 assembly and neurotoxicity, manuscript in preparation), indicating that the mechanism of A $\beta$ 42 toxicity inhibition by A $\beta$ (30–40) may be similar to that of A $\beta$ (39–42). Taken together, the data suggest that inhibition is structure-specific rather than based on

generic hydrophobic association. To obtain a better understanding of the inhibition mechanisms of the assembly and toxicity of full-length A $\beta$ 42 by CTFs, we conducted a detailed study of the structures of the CTFs themselves.

Here, we have applied replica exchange molecular dynamics (REMD)<sup>23–26</sup> with an explicit solvent to probe the structures of selected CTFs [A $\beta$ ( $x$ -42);  $x$ =29–31, 39]. In addition, solvent-free simulations of A $\beta$ ( $x$ -42) ( $x$ =29–39) were performed for comparison with ion mobility mass spectrometry (IM-MS),<sup>10,27,28</sup> a powerful tool used for investigating the structure of biological molecules, including A $\beta$ 42.<sup>10</sup> The roles of the structures of the CTFs in disrupting oligomerization and inhibiting A $\beta$ 42-induced neurotoxicity are discussed.

## Results

### Ion mobility and solvent-free structures of CTFs

REMD solvent-free simulations with a cumulative time of 320 ns ( $16 \times 20$  ns) were conducted for each of the CTFs [A $\beta$ ( $x$ -42);  $x$ =29–39]. In order to characterize the secondary structural features of each fragment, secondary structural propensity was calculated from the last 10-ns trajectory at 300 K, as described in **Materials and Methods**. Results of this analysis are shown in Supplementary Material (**Fig. S1**). No  $\beta$ -sheet propensity (0%) is present in any fragment. Turn (~72%) and coiled conformation (~24%) are dominant for every fragment, and  $\alpha$ -helical propensity (~10%) exists only for the three longest fragments [A $\beta$ ( $x$ -42);  $x$ =29–31]. To further characterize the tertiary fold, the major structural families of each fragment were obtained by applying the pairwise GROMOS clustering method<sup>29</sup> on the last 10-ns trajectory at 300 K. The abundance and representative structure of each structural family are presented in **Fig. S2** of **Supplementary Material**. In summary, the two predominant conformations for each of the three longest fragments [A $\beta$ ( $x$ -42);  $x$ =29–31] are a U-shape fold and a turn-coil conformation. Two medium-length fragments [A $\beta$ ( $x$ -42);  $x$ =32–33] primarily adopt only a turn-coil conformation. The remaining short fragments [A $\beta$ ( $x$ -42);  $x$ =34–39] mainly adopt a turn conformation. To compare with experimental data, the cross section of each representative structure was calculated and listed in **Table S1**.

Mass spectra and arrival time distributions (ATDs) were obtained for each of the CTFs [A $\beta$ ( $x$ -42);  $x$ =29–39], and experimental cross sections were calculated from the ATDs (see **Figs. S3–S5** and **Tables S1** and **S2** in **Supplementary Material** for details). The cross sections from the REMD simulations generally agree well with experimental values, as shown in **Fig. 1** (numerical values are listed in **Table S1**). The calculated values are within experimental uncertainty ( $\pm 2\%$ ) for all CTFs, except for A $\beta$ (31–42) ( $\pm 5\%$ ) and A $\beta$ (36–42) ( $\pm 10\%$ ). In addition, multiple

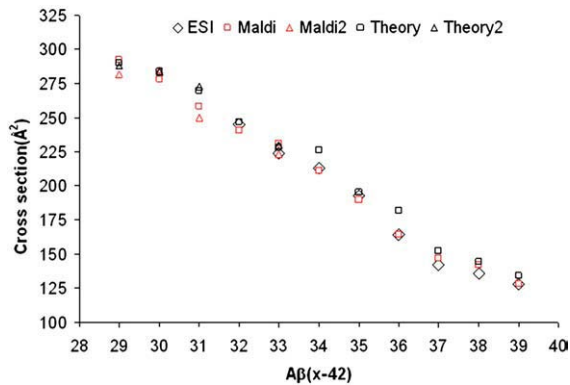


**Fig. 1.** A comparison of cross-sectional data from ion mobility experiments and REMD calculations. Experimental data were taken with both a nano-ESI source [black diamond; only available for A $\beta$ (x-42); x=32-39] and a MALDI source (red square). In some cases, a second feature was seen in MALDI spectra, indicated by MALDI2 (red triangle). In these cases, cross sections were calculated for representative structures of the first and second clusters, as indicated by Theory (black square) and Theory 2 (black triangle), respectively.

features in the ATDs correlate directly with the theoretical results (Fig. S5), pointing to the ability of theory to predict relevant peptide structures that exist in the experiment.

### Solution structures of A $\beta$ 42 CTFs

Four CTFs [A $\beta$ (29-42), A $\beta$ (30-42), A $\beta$ (31-42), and A $\beta$ (39-42)] were selected for further analysis with REMD simulations in water to probe their solution structures. The most populated structures obtained from the solvent-free REMD simulations (Fig. 2) were solvated in water and used as initial structure for REMD simulations with explicit water. REMD simulations with a cumulative time of 800 ns (40  $\times$  20 ns) were conducted for each CTF. The secondary structural propensity was calculated from the last 10-ns trajectory at 300 K (see Fig. 3). Based on main-chain  $\varphi$  and  $\psi$  torsion angles, 55%, 10%, and 35% of the residues in the conformational ensemble of the shortest fragment A $\beta$ (39-42) are in  $\beta$ -extended,  $\alpha$ -helical, and coiled conformation, respectively. In comparison with its solvent-free propensities (0%, 43%, and 56% for  $\beta$ -extended,  $\alpha$ -helical, and coiled conformation, respectively), the solvent environment significantly populates the

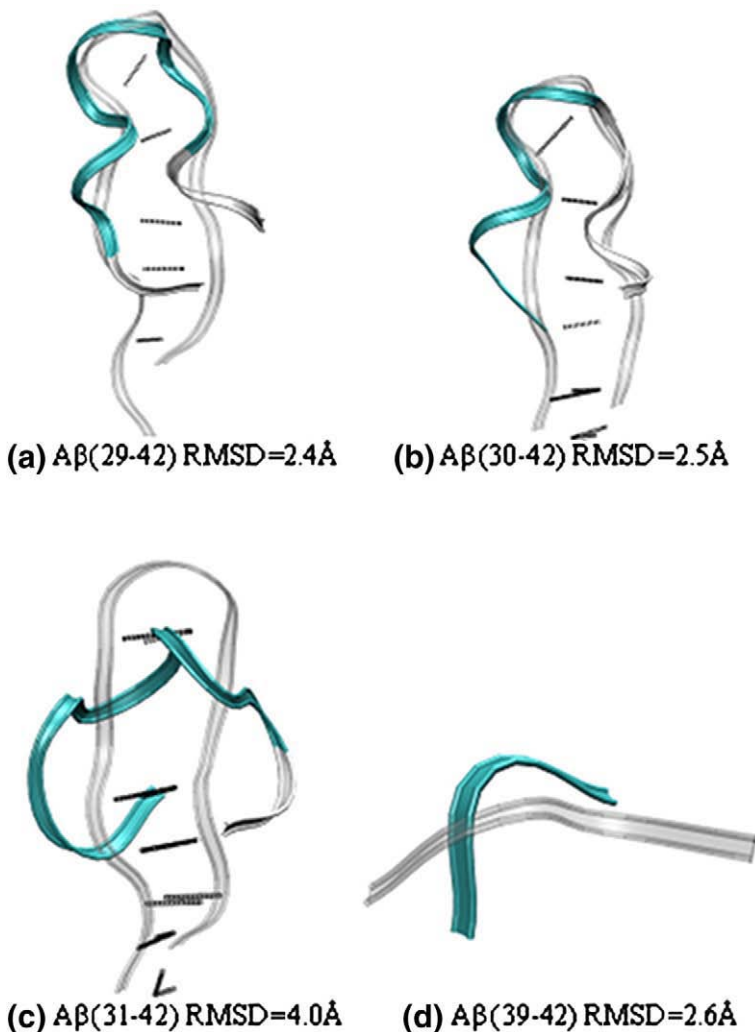


**Fig. 2.** Overlap of the solvent-free structure (represented by a color ribbon: coil in silver and turn in cyan) and the solution-phase structure (silver ribbon) of selected CTFs at 300 K. The root mean square distance of the solvent-free structure from the solution structure is given under each structure. The cross-strand main-chain hydrogen bonds in the solution structures are shown with a dashed line.

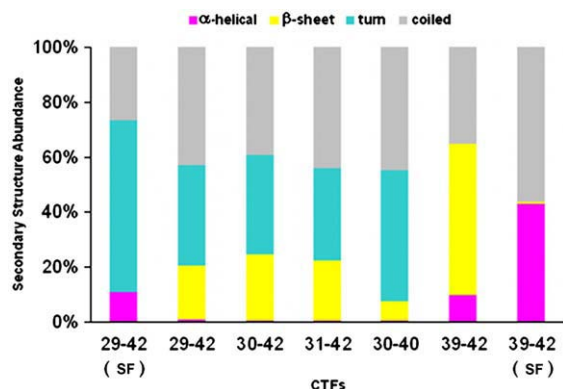


**Fig. 3.** Secondary structure abundance of A $\beta$ (29–42), A $\beta$ (30–42), A $\beta$ (31–42), A $\beta$ (30–40), and A $\beta$ (39–42) in water, as well as A $\beta$ (29–42) and A $\beta$ (39–42) in a solvent-free environment (SF) at 300 K. STRIDE was used to classify the peptides, except for A $\beta$ (39–42), which was classified by a “course-grained” scheme based on main-chain  $\varphi$  and  $\psi$  torsion angle combinations.

$\beta$ -conformation (i.e., from 0% to 55%). Similar trends exist for the three longest CTFs [A $\beta$ ( $x$ –42);  $x$  = 29–31]. As a representative example, the  $\beta$ -sheet propensity of A $\beta$ (29–42) increases from 0% in the solvent-free environment to 20%,  $\alpha$ -helical propensity decreases from 11% to 1%, and propensity for turn or coil conformation decreases from 90% to 80%.

To characterize the tertiary fold in water, the 10 most populated clusters of each peptide [A $\beta$ (29–42), A $\beta$ (30–42), A $\beta$ (31–42), and A $\beta$ (39–42)] were obtained by applying the pairwise GROMOS clustering method to the last 10-ns trajectory at 300 K. The most populated clusters (see Fig. S6 in Supplementary Material) were further merged into two superclusters: those with a  $\beta$ -hairpin or extended  $\beta$ -strand, and those with a turn-coil conformation. The abundance and representative structures of the two superclusters are presented in Fig. 4. A $\beta$ (29–42), A $\beta$ (30–42), and A $\beta$ (31–42) have moderate tendencies to adopt  $\beta$ -hairpin structures rather than turn-coil conformations. It is also important to note that the abundance of  $\beta$ -hairpin decreases with CTF length. For example, 43% of the conformation ensemble of A $\beta$ (29–42) is on  $\beta$ -hairpin conformation, whereas only 25% of A $\beta$ (31–42) molecules adopt a similar structure. The shortest CTF A $\beta$ (39–42) has a 71% structural abundance of a  $\beta$ -extended strand and an 11% structural abundance of turn.

Figure 2 offers a direct comparison between solution-phase and solvent-free CTF structures. When solvated in water, A $\beta$ (29–42) and A $\beta$ (30–42) retain the U-shape topology, whereas A $\beta$ (31–42) and A $\beta$ (39–42) change topology. Overall, the water solvent environment significantly favors  $\beta$ -hairpin and  $\beta$ -extended conformations. For A $\beta$ (29–42) and A $\beta$ (30–42), two twisted strands with helical turn conformations exist in the solvent-free structures. These are converted into extended  $\beta$ -strands in the solution structures, and local hydrogen bonds in the helical turns are replaced by cross-strand hydro-

gen bonds. For A $\beta$ (31–42), the trend is even more dramatic, as a coiled conformation is converted into a  $\beta$ -hairpin upon solvation. The data demonstrate that hydrophobic interactions, which exist in water but not in vacuum, are required for the cross-strand hydrogen bonds of the  $\beta$ -hairpin to exist. For A $\beta$ (39–42), a turn conformation becomes a  $\beta$ -extended conformation upon solvation (Fig. 2). This may be explained by the screening effect of polar water molecules that reduce electrostatic interactions between termini.

In order to probe the role of the last two hydrophobic residues (IA) in stabilizing the  $\beta$ -hairpin conformation of A $\beta$ (30–42), REMD simulations starting from the truncated  $\beta$ -hairpin structure of A $\beta$ (30–42) were carried out for a cumulative time of 800 ns. The results of secondary structural analysis show that the  $\beta$ -sheet propensity of A $\beta$ (30–40) is 7%, three times as low as that of A $\beta$ (30–42). The propensity for a coiled or turn structure is 92% in A $\beta$ (30–40), compared to 75% in A $\beta$ (30–42) (Fig. 3). Overall, A $\beta$ (30–40) predominantly adopts a turn-coil structure (Fig. 4g) rather than the  $\beta$ -hairpin conformation seen in A $\beta$ (30–42) (Fig. 4c).

## Discussion and Conclusions

Previous studies<sup>6,7,15,17,19–21</sup> have pointed to the existence of metastable structures in the C-terminus of A $\beta$ 42, although few have provided all-atom structures. Here, we conduct a detailed structural study combining experimental and theoretical results and gain a more in-depth understanding of the forces governing the  $\beta$ -structuring of the A $\beta$ 42 C-terminus. A positive correlation between the hydrophobicity of the C-terminus of A $\beta$  and its ability to form ordered aggregates has already been established. For example, when hydrophilic residues were introduced at positions I41 and A42, A $\beta$ 42 was less prone to assembly than wild-type A $\beta$ 40,<sup>30</sup> whereas substitutions with residues exhibiting greater hydrophobicity were more prone to assembly than A $\beta$ 42.<sup>30,31</sup> Still, it remains unclear why these hydrophobic residues promote ordered assembly (e.g.,  $\beta$ -sheet) rather than disordered assembly if driven only by nonspecific hydrophobic interactions. Here, we demonstrate that the increased hydrophobicity due to the IA residues promotes  $\beta$ -hairpin formation in A $\beta$ 42. In turn, metastable  $\beta$ -hairpin may promote ordered oligomerization/ $\beta$ -sheet formation of A $\beta$ 42, which may be more toxic than disordered oligomers by A $\beta$ 40. Thus, the hydrophobic interactions may stabilize cross-strand hydrogen bonds and thereby increase the formation of ordered toxic structures.

The solution-phase REMD simulations indicate the presence of a metastable  $\beta$ -hairpin structure for A $\beta$ ( $x$ –42) ( $x$  = 29–31). Secondary structure analysis shows a notable abundance of turn (~35%) and  $\beta$ -sheet (~20%) within these peptides in water solvent (Fig. 3). The  $\beta$ -turn in the hairpin-like structure generally consists of four residues with a varied

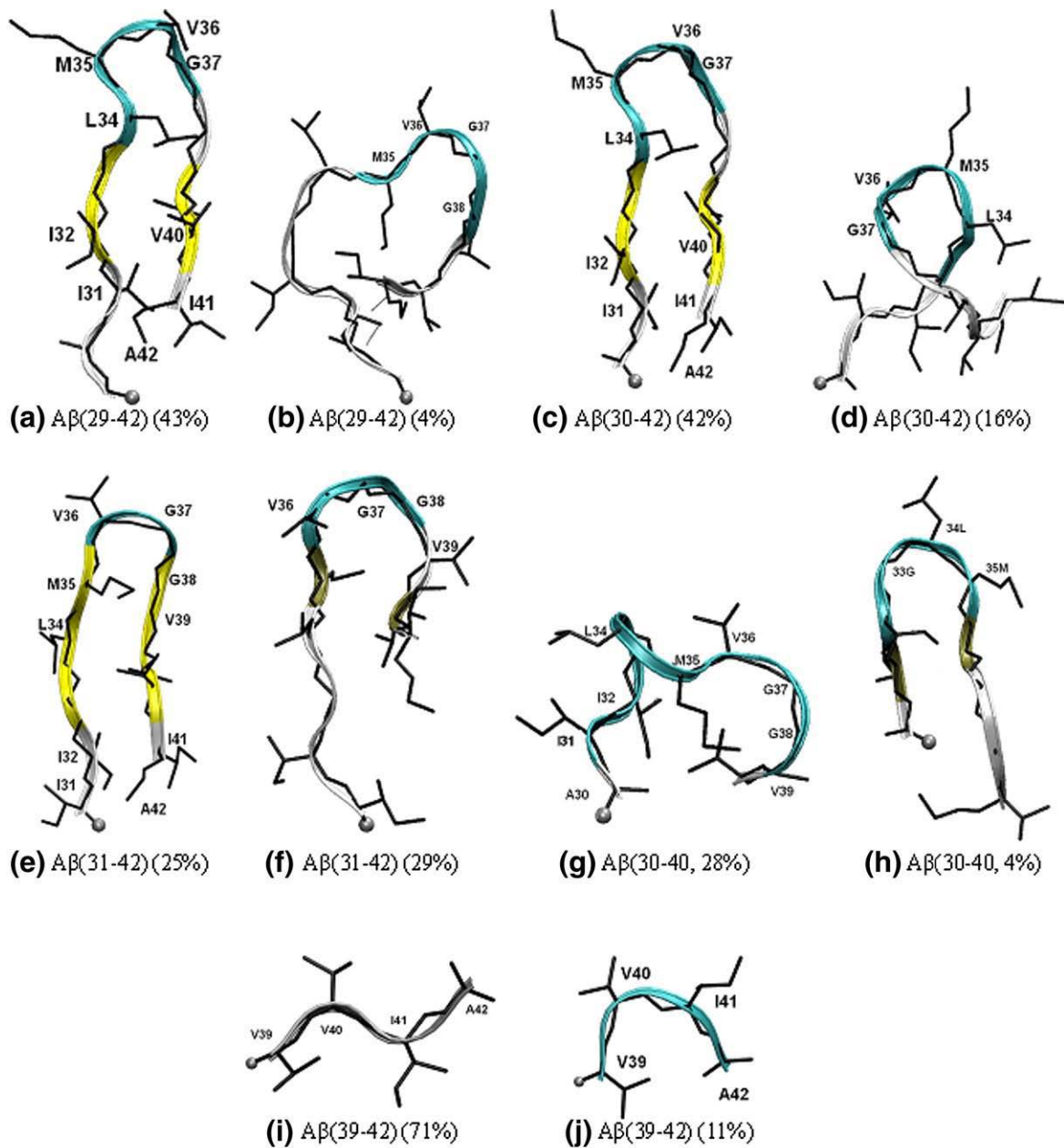


**Fig. 4.** Representative structures of superclusters (hairpin-like and non-hairpin-like) of each CTF from simulations in water at 300 K. The backbone is shown in cartoon. Secondary structure is coded by color: coil in silver,  $\beta$ -sheet in yellow, isolated  $\beta$ -bridge in tan, and turn in cyan. The N-terminus is indicated by a ball. The abundance of each supercluster (sum of the abundance of each cluster in a supercluster in Fig. S6) is given in parentheses.

location (residues 34–37/LMVG, residues 35–38/MVGG, or residues 36–39/VGGV). Similar results were obtained in two discrete molecular dynamics (MD) studies of full-length A $\beta$ 42 folding in implicit solvent, which showed a turn at residues G37 and G38.<sup>6,7</sup> Although the location of the turn changes slightly among the structures presented here, the turn always includes one or two glycine residue(s). Glycine is often found in turns because of its very low barrier for rotating  $\varphi$  or  $\psi$  torsion angles into turn regions. The two  $\beta$ -strands in the hairpin-like structures are stabilized by hydrophobic interactions between side chains, cross  $\beta$ -strand main-chain

hydrogen bonds, and van der Waals interactions (Fig. 4).

Our results on CTFs further suggest that the forces critical for forming the turn and  $\beta$ -strand are distinct: the former can be stabilized in solvent-free environment by electrostatic interactions and van der Waals interactions within the peptide, whereas the latter requires the additional contribution of hydrophobic interactions provided by a water solvent environment. For example, solvent-free simulations show that as water solvent is removed, the turn population increases, possibly by enhanced electrostatic interactions, and the  $\beta$ -sheet conformation disappears,

due to loss of hydrophobic interactions [Fig. 3 for A $\beta$ (29–42)]. On the other hand, upon solvation, hydrophobic clusters help to stabilize the cross-strand main-chain hydrogen bonds that are crucial in forming the  $\beta$ -hairpin. For example, in supercluster C1 of A $\beta$ (29–42) in water (see Fig. 4a), main-chain hydrogen bonds between two  $\beta$ -strands are stabilized by hydrophobic clusters (L34-I32-V40 and I31-V41). In contrast, in the solvent-free environment,  $\alpha$ -helical or turn conformations dominate, stabilized by short-range hydrogen bonds. It is clear that hydrophobic forces are essential in maintaining the  $\beta$ -hairpin structure, which is consistent with previous theoretical studies on other peptide systems.<sup>32–34</sup>

Considering the importance of hydrophobic interactions in maintaining the  $\beta$ -hairpin of A $\beta$ (30–42), it is not surprising that the absence of the two C-terminal hydrophobic residues (IA) causes a significant structural change. Our results show that the  $\beta$ -hairpin is almost completely absent in A $\beta$ (30–40) (Fig. 4h) and, instead, the predominant conformations of A $\beta$ (30–40) are in a turn-coil conformation (Fig. 4g). This dramatic change points to a similar structural difference between full-length A $\beta$ 42 and A $\beta$ 40. The metastable  $\beta$ -strand or  $\beta$ -hairpin in the C-terminus may help seed aggregation of the peptide<sup>14,15</sup> and/or make aggregation entropically favorable.<sup>5,15,16</sup>

Based on ensemble experiments, A $\beta$ 42 monomer is believed to adopt a collapsed-coil structure<sup>35</sup> with metastable local structural elements. All-atom simulations<sup>10,36</sup> and selective experiments<sup>10,37</sup> have shown that local structural elements, including a bend region (A $\beta$ 22–28) stabilized by a K28-D23 salt bridge and the central hydrophobic core (A $\beta$ 17–21), play important roles in the  $\beta$ -structuring of A $\beta$ . Along this same line, our results underline the importance of I41 and A42 in creating the  $\beta$ -structure of the C-terminus of A $\beta$ 42. This  $\beta$ -structuring correlates with the role of these two residues in supporting paranucleus formation by A $\beta$ 42, but not by A $\beta$ 40,<sup>9,31</sup> as well as the higher toxicity of oligomers of A $\beta$ 42 relative to those of A $\beta$ 40.<sup>11</sup>

Our study reveals an intriguing length dependence on the propensity for forming  $\beta$ -hairpin by the CTFs. While A $\beta$ (29–42) and A $\beta$ (30–42) have similar  $\beta$ -hairpin propensities (~40%), shortening the sequence by just one residue to A $\beta$ (31–42) reduces the  $\beta$ -hairpin propensity almost by half (to ~25%). Even more striking is that the removal of the last two residues of A $\beta$ (30–42) changes the  $\beta$ -hairpin propensity from ~40% to ~0%. This length dependence may partially explain the differences in the ability of these CTFs to disrupt oligomerization and to inhibit A $\beta$ 42-induced neurotoxicity.

Fradinger *et al.* hypothesized that molecules with a high affinity for the C-terminus of A $\beta$ 42 would disrupt A $\beta$ 42 oligomerization and inhibit A $\beta$ 42-induced neurotoxicity.<sup>22</sup> Fragments of the C-terminus of full-length A $\beta$ 42 proved to be good candidates. A higher inhibitory activity of some CTFs compared to others suggests that inhibition is structure-specific rather than based on generic hydrophobic association.

Inhibition of paranucleus formation was strongest for A $\beta$ (29–42) and decreased upon shortening of the sequence to A $\beta$ (30–42) and A $\beta$ (31–42).<sup>22</sup> This result correlates with the decrease in the extent of the  $\beta$ -hairpin conformation observed in the results of our REMD simulations. In contrast, inhibition of A $\beta$ -induced toxicity increased from A $\beta$ (29–42) to A $\beta$ (31–42), correlating with the increase in the abundance of coil-turn conformations displayed by these CTFs. Moreover, A $\beta$ (30–40), which was found to be predominantly in a coil-turn conformation, was a strong inhibitor of A $\beta$ -induced toxicity (H. Li, B. H. Monien, A. Lomakin, E. A. Fradinger, S. M. Spring, B. Urbanc, G. B. Benedek & G. Bitan, Mechanistic investigation of C-terminal fragments as inhibitors of A $\beta$ 42 assembly and neurotoxicity, manuscript in preparation). It is therefore tempting to speculate that the inhibition of paranucleus formation and A $\beta$ 42-induced toxicity correlate with the tendencies of these CTFs to adopt  $\beta$ -hairpin and coil-turn conformations, respectively. The data suggest that subtle structural differences among A $\beta$ (29–42), A $\beta$ (30–42), and A $\beta$ (31–42) at the monomer level lead to differences in each CTF's folding, self-assembly, and coassembly with full-length A $\beta$ 42, resulting in different inhibitory activities. The potent inhibitory activity of A $\beta$ (39–42) likely is achieved by mechanisms or interactions that are distinct from those of 12- to 14-residue CTFs. A $\beta$ (39–42) adopts a metastable extended  $\beta$ -conformation, which may play a role in binding to full-length A $\beta$ 42 and in interrupting intramolecular interactions within A $\beta$ 42 monomers. Currently, IM-MS studies are underway to investigate mixtures of A $\beta$ 42 and various CTFs.

## Materials and Methods

### Sample preparation

All CTFs ( $x$ -42, where  $x$  ranges from 29 to 39) of A $\beta$ 42 [DAEFRHDSGY<sub>10</sub>EVHHQKLVFF<sub>20</sub>AEDVGSNKG<sub>A30</sub>IIGLMVGGVV<sub>40</sub>IA] were synthesized using *N*-(9-fluorenyl)methoxycarbonyl chemistry, purified by reverse-phase HPLC, and characterized by mass spectrometry and amino acid analysis as described previously.<sup>38</sup>

For IM-MS analysis, samples were dissolved in 5.8% NH<sub>4</sub>OH and diluted in 20 mM NH<sub>4</sub>OAc (pH 7.4) to make a 10  $\mu$ M solution of peptide. Between 2 and 5  $\mu$ l of the sample solution was placed into nano-electrospray ionization (nano-ESI) gold-coated borosilicate capillaries (outer diameter, 0.1 mm; inner diameter, 0.78 mm) purchased from Proxeon (Germany) for delivery into the instrument. For analysis with a matrix-assisted laser desorption/ionization (MALDI) source, samples were dissolved in hexafluoroisopropanol, and 2,5-dihydroxybenzoic acid was added as matrix to the solution.

### Instrumental setup

Ion mobility measurements were recorded on two home-built instruments. The first instrument has a nano-ESI source. Droplets containing the CTFs are sprayed from this source. Peptide ions pass through a capillary and

travel through an ion funnel where they are dehydrated and stored. From the ion funnel, the ions enter a 5-cm temperature-controlled drift cell that is filled with  $\sim 5$  Torr of helium. For mass spectrometry measurements, the ions pass through the drift cell into a quadrupole mass filter where they are mass-selected and continue to the detector. For ion mobility measurements, ions stored in the ion funnel are pulsed into the drift cell. Ions travel through the drift cell under the influence of a weak electric field. Exiting the drift cell, the ions are mass-selected and detected, creating an ATD. A more detailed explanation of the instrument configuration has been published elsewhere.<sup>10</sup>

Three CTFs, A $\beta$ (29–42), A $\beta$ (30–42), and A $\beta$ (31–42), are hardly soluble in aqueous buffers.<sup>22,38</sup> These peptides aggregated quickly and clogged the nano-electrospray tips. Therefore, ion mobility measurements were also recorded using a MALDI time-of-flight instrument. Here, the sample is inserted into the MALDI source, where it is desorbed and ionized by a nitrogen laser. For mobility measurements, a linear mass gate is turned on, and the time-of-flight reflectron is turned off so that the ions may travel through to the drift cell. The cylindrical glass drift cell is 20 cm long and filled with  $\sim 1.5$  Torr of helium. Once through the drift cell, ions pass through a quadrupole mass filter and are detected as a function of time, yielding an ATD of a given ion. A more thorough explanation of this instrument may be found elsewhere.<sup>39</sup>

### Ion mobility measurements

The time it takes for an ion to drift through the cell  $t_d$  is inversely proportional to the cell length  $\ell$  and the electric field  $E$ . The proportionality constant is  $(K)^{-1}$ , where  $K$  is termed ion mobility:

$$t_d = t_A - t_0 = (\ell EK)^{-1} = \frac{\ell^2}{K_0} \frac{237.16 p}{760T V} \quad (1)$$

where  $V$  is the cell voltage ( $E=V/\ell$ ) and  $K_0$  is the mobility at standard temperature and pressure. In Eq. (1), the pressure  $p$  is expressed in Torr and the temperature  $T$  is expressed in Kelvin.  $K_0$  is determined from the slope of a plot of arrival time  $t_A$  versus  $p/V$  for a series of voltages, and the time outside the cell  $t_0$  is the intercept. The value of  $K_0$  obtained from such a plot is inversely proportional to the collision cross section  $\sigma$  ( $\text{\AA}^2$ ), which yields the averaged cross section of the ion of interest:

$$\sigma = \frac{A}{k_0} \quad (2)$$

where  $A$  is a collection of known constants and system parameters obtained from kinetic theory.<sup>40</sup> The collision cross section reflects the dimensions of the molecule.

### Molecular modeling

All REMD simulations were performed using the GROMACS simulation package.<sup>41</sup> Gas-phase REMD simulations were carried out for all CTFs [A $\beta$ ( $x$ –42);  $x=29$ –39)] for comparison to IM-MS data. The AMBER94 force field<sup>42</sup> was selected to model the peptides in gas phase because AMBER94 performed better than GROMOS96<sup>43</sup> and OPLS-AA<sup>44</sup> in modeling A $\beta$ (21–30) gas-phase structures.<sup>37</sup> GROMACS ports of AMBER force fields were provided by Sorin and Pande.<sup>45</sup> Sixteen replicas of the peptide system in the gas phase were simulated at temperatures exponentially spaced from 300 to 2200 K (i.e., 300.0, 342.6, 391.3,

446.9, 510.4, 582.8, 665.6, 760.2, 868.2, 991.5, 1132.4, 1293.2, 1476.9, 1686.7, 1926.4, and 2200.0 K; see below for the algorithm used to determine them). An extremely high temperature (i.e., up to 2200 K) was used to overcome slow structural relaxation in the gas phase. We verified that the high temperatures used in our simulations did not produce any notable structural artifact such as *trans-to-cis* isomerizations of the peptide bonds within the duration of the simulations (20.0 ns). Replica exchange trials between neighboring pairs were attempted every 250 MD steps (0.5 ps). The average exchange probability was  $\sim 13\%$ . The simulations were started from an extended conformation. The simulation length was 20.0 ns for each replica, resulting in 320.0 ns of accumulated simulation time for each peptide. The nonbonded Lennard–Jones potential was normal out to 15.0  $\text{\AA}$ , after which it was switched off to reach zero at 25.0  $\text{\AA}$ . A cutoff of 40.0  $\text{\AA}$  was set for the long-range electrostatic interactions. The centers of mass translation and rotation were removed every 1000 steps. Neighbor lists for nonbonded interactions were updated every 10 simulation steps. The temperature was controlled by a Nose–Hoover thermostat<sup>46</sup> with a 0.05-ps time constant. The LINCS protocol<sup>47</sup> was used to constrain all bonds involving hydrogen atoms. A shorter time step of 0.5 fs, rather than the typical 2.0 fs, was used to avoid the LINCS failure associated with large atomic displacements at the high temperatures used in our simulations (up to 2200 K leading to a higher kinetic velocity).

The most populated structure of each of the four CTFs A $\beta$ (29–42), A $\beta$ (30–42), A $\beta$ (31–42), and A $\beta$ (39–42) obtained from the gas-phase REMD simulations was used as an initial structure for REMD simulations with explicit water solvent. The initial structure for simulating A $\beta$ (30–40) in water was obtained from the most populated solution structure ( $\beta$ -hairpin) of A $\beta$ (30–42) by removing the last two residues. Since the OPLS-AA force field<sup>44</sup> performs better in modeling A $\beta$  in a condensed phase than GROMOS96 or AMBER94,<sup>21,48</sup> OPLS-AA was used to model these five CTFs in water. The initial peptide structure was solvated in an octahedron box (42–52  $\text{\AA} \times 39$ –49  $\text{\AA} \times 34$ –42  $\text{\AA}$  of an equivalent triclinic box) filled with TIP3P water molecules,<sup>2</sup> and the peptide was positioned 15  $\text{\AA}$  away from the box wall. There were 3146, 3606, 3123, 3404, and 1885 water molecules for A $\beta$ (30–40), A $\beta$ (29–42), A $\beta$ (30–42), A $\beta$ (31–42), and A $\beta$ (39–42), respectively. Forty replicas of the peptide system in water were simulated in each case at temperatures exponentially spaced from 300 to 600 K (i.e., 300.0, 305.4, 310.9, 316.4, 322.1, 327.9, 333.8, 339.7, 345.8, 352.0, 358.4, 364.8, 371.3, 377.9, 384.7, 391.6, 398.6, 405.8, 413.1, 420.5, 428.0, 435.7, 443.5, 451.4, 459.5, 467.8, 476.2, 484.7, 493.4, 502.3, 511.3, 520.4, 529.8, 539.3, 548.9, 558.8, 568.8, 579.0, 589.4, and 600.0 K; see below for the algorithm used to determine them). Replica exchange trials between neighboring pairs were attempted every 250 MD steps (0.5 ps). The average exchange probability was  $\sim 20\%$ . A short 0.2-ns MD simulation at 300 K in the NPT ( $n$  particles, constant pressure and temperature) ensemble was performed to equilibrate the system. Then, REMD simulations were performed for 20.0 ns in the NVT ( $n$  particles, constant volume and temperature) ensemble, resulting in an aggregation time of 800.0 ns for each peptide system. A time step of 2.0 fs was used. The nonbonded Lennard–Jones potential was normal out to 10.0  $\text{\AA}$ , after which it was switched off to reach zero at 11.0  $\text{\AA}$ . The particle-mesh Ewald method<sup>49</sup> was used to treat the long-range electrostatic interactions. The other simulation protocols such as thermostat, restraints on bonds involving hydrogen atoms, and so on were the same as those in the solution-phase simulations.

## Structural analysis

For analysis of secondary structure, the STRIDE program of Frishman and Argos was used whenever possible (i.e., the peptide contains more than five residues).<sup>50</sup> In the case of A $\beta$ ( $x$ -42) ( $x$ =38, 39), a coarse-grained scheme based on main-chain  $\varphi$  and  $\psi$  torsion angle combinations was used instead: right-handed helical conformation was assigned to regions where  $-140^\circ < \varphi < -30^\circ$  and  $-90^\circ < \psi < 45^\circ$ ;  $\beta$ -extended conformation was assigned to regions where  $-180^\circ < \varphi < -30^\circ$ ,  $60^\circ < \psi < 180^\circ$ , and  $-180^\circ < \psi < -150^\circ$  and to coiled regions where the values of  $\varphi$  and  $\psi$  are outside of these regions. For analysis of tertiary structure, the snapshots of the ensemble were clustered by the GROMACS protocol,<sup>29</sup> in which the structure similarity score is based on pairwise root mean square distance over C $^\alpha$  atoms of the peptide. This was performed in order to reduce a large number of the sampled structures into a few structure families. The structure that has the largest number of neighboring structures within the cutoff [1.0 Å for A $\beta$ ( $x$ -42),  $x$ =29–34 or 0.5 Å for  $x$ =35–39] was selected as the representative structure of the structure cluster. The representative structure of the structure family was used to calculate the cross section by a trajectory method<sup>51,52</sup> for solvent-free simulations.

## Convergence of REMD

The convergence of the REMD simulation was rigorously checked by block analysis: the total 20.0-ns sampling at 300 K was divided into four blocks of 5.0 ns, and the secondary structure and tertiary structure clustering analysis detailed above was performed for each block. For all sets of REMD simulations, a good convergence was found during the last 10 ns [e.g., see the data for A $\beta$ (30–42) in Fig. S7 of Supplementary Material]. The structural results presented in this work were calculated from the last 10-ns trajectory at 300 K.

## Algorithm for determining the temperature distribution for REMD

Temperature distribution is optimized to yield a good energy overlap between two neighboring replicas at temperatures  $T_i$  and  $T_{i+1}$  ( $T_0$  is equal to the lowest temperature given  $T_{\min}$ ). In other words, the mean energy gap between the two neighboring replicas  $\Delta E_{i,i+1}$  is set to be comparable to the energy fluctuation  $\delta E_i$  of replica  $i$ , that is,

$$\frac{\Delta E_{i,i+1}}{\delta E_i} = 1 \quad (3)$$

The energy distribution of replica  $i$  at temperature  $T_i$  is approximated by a Gaussian distribution model with two parameters: a mean energy  $E_i$  and a spontaneous energy fluctuation  $\delta E_i$ . The mean energy  $E_i$  is proportional to the product of temperature  $T_i$  and to the number of degrees of freedom  $f$  of the simulated system, leading to the following expression for the mean energy gap between two neighboring replicas:

$$\Delta E_{i,i+1} \propto \Delta T_{i,i+1} * f \quad (4)$$

The standard energy fluctuation  $\delta E_i$  is proportional to the product of the temperature  $T_i$  and the square root of  $f$ :

$$\delta E_i \propto T_i * \sqrt{f} \quad (5)$$

By substituting Eqs. (4) and (5) into Eq. (3), the optimized temperature gap between the two neighboring replicas is obtained as:<sup>53</sup>

$$\Delta T_{i,i+1} = \frac{T_i}{\sqrt{f}} \quad (6)$$

The total number of replicas is determined from the highest temperature  $T_{\max}$ . Finally, the temperature distribution is manually fine-tuned to obtain an average exchange probability of  $\sim 10$ –20% based on a short REMD trial.

## Acknowledgements

The support of National Institute of Health grant IPOIAG027818 (M.T.B. and G.B.), the David and Lucile Packard Foundation (J.-E.S.), National Science Foundation grants CHE-0503728 (M.T.B.) and MCB-0642088 (J.-E.S.), and Larry L. Hillblom Foundation grant 2005/2E (G.B.), and a generous gift from the Turken family (G.B.) are gratefully acknowledged. Simulations were performed on the Lonestar cluster at the Texas Advanced Computing Center (LRAC MCA05S027 to J.-E.S.).

## Supplementary Data

Supplementary data associated with this article can be found, in the online version, at doi:10.1016/j.jmb.2009.01.029

## References

1. Kirkitadze, M. D., Bitan, G. & Teplow, D. B. (2002). Paradigm shifts in Alzheimer's disease and other neuro degenerative disorders: the emerging role of oligomeric assemblies. *J. Neurosci. Res.* **69**, 567–577.
2. Jorgensen, W. L., Chandrasekhar, J., Madura, J. D., Impey, R. W. & Klein, M. L. (1983). Comparisons of simple potential functions for simulating liquid water. *J. Chem. Phys.* **79**, 926–935.
3. Shankar, G. M., Li, S. M., Mehta, T. H., Garcia-Munoz, A., Shepardson, N. E., Smith, I. *et al.* (2008). Amyloid- $\beta$  protein dimers isolated directly from Alzheimer's brains impair synaptic plasticity and memory. *Nat. Med.* **14**, 837–842.
4. Lesne, S., Koh, M. T., Kotilinek, L., Kaye, R., Glabe, C. G., Yang, A. *et al.* (2006). A specific amyloid- $\beta$  protein assembly in the brain impairs memory. *Nature*, **440**, 352–357.
5. Roberson, E. D., Scarce-Levie, K., Palop, J. J., Yan, F. R., Cheng, I. H., Wu, T. *et al.* (2007). Reducing endogenous tau ameliorates amyloid beta-induced deficits in an Alzheimer's disease mouse model. *Science*, **316**, 750–754.
6. Urbanc, B., Cruz, L., Yun, S., Buldyrev, S. V., Bitan, G., Teplow, D. B. & Stanley, H. E. (2004). *In silico* study of amyloid  $\beta$ -protein folding and oligomerization. *Proc. Natl Acad. Sci. USA*, **101**, 17345–17350.
7. Yun, S. J., Urbanc, B., Cruz, L., Bitan, G., Teplow, D. B. & Stanley, H. E. (2007). Role of electrostatic inter-

- actions in amyloid  $\beta$ -protein (A $\beta$ ) oligomer formation: a discrete molecular dynamics study. *Biophys. J.* **92**, 4064–4077.
8. Lazo, N. D., Grant, M. A., Condron, M. C., Rigby, A. C. & Teplow, D. B. (2005). On the nucleation of amyloid  $\beta$ -protein monomer folding. *Protein Sci.* **14**, 1581–1596.
  9. Bitan, G., Kirkitadze, M. D., Lomakin, A., Vollers, S. S., Benedek, G. B. & Teplow, D. B. (2003). Amyloid  $\beta$  protein (A $\beta$ ) assembly: A $\beta$ 40 and A $\beta$ 42 oligomerize through distinct pathways. *Proc. Natl Acad. Sci. USA*, **100**, 330–335.
  10. Bernstein, S. L., Wyttenbach, T., Baumketner, A., Shea, J. E., Bitan, G., Teplow, D. B. & Bowers, M. T. (2005). Amyloid beta-protein: monomer structure and early aggregation states of A beta 42 and its Pro(19) alloform. *J. Am. Chem. Soc.* **127**, 2075–2084.
  11. Dahlgren, K. N., Manelli, A. M., Stine, W. B., Baker, L. K., Krafft, G. A. & LaDu, M. J. (2002). Oligomeric and fibrillar species of amyloid- $\beta$  peptides differentially affect neuronal viability. *J. Biol. Chem.* **277**, 32046–32053.
  12. Borchelt, D. R., Thinakaran, G., Eckman, C. B., Lee, M. K., Davenport, F., Ratovitsky, T. *et al.* (1996). Familial Alzheimer's disease-linked presenilin 1 variants elevate A $\beta$  1–42/1–40 ratio *in vitro* and *in vivo*. *Neuron*, **17**, 1005–1013.
  13. Jarrett, J. T., Berger, E. P. & Lansbury, P. T. (1993). The carboxy terminus of the  $\beta$ -amyloid protein is critical for the seeding of amyloid formation—implications for the pathogenesis of Alzheimer's disease. *Biochemistry*, **32**, 4693–4697.
  14. Sawaya, M. R., Sambashivan, S., Nelson, R., Ivanova, M. I., Sievers, S. A., Apostol, M. I. *et al.* (2007). Atomic structures of amyloid cross-beta spines reveal varied steric zippers. *Nature*, **447**, 453–457.
  15. Yan, Y. L. & Wang, C. Y. (2006). A $\beta$  42 is more rigid than A $\beta$  40 at the C terminus: implications for A $\beta$  aggregation and toxicity. *J. Mol. Biol.* **364**, 853–862.
  16. Thirumalai, D., Klimov, D. K. & Dima, R. I. (2003). Emerging ideas on the molecular basis of protein and peptide aggregation. *Curr. Opin. Struct. Biol.* **13**, 146–159.
  17. Lim, K. H., Collver, H. H., Le, Y. T. H., Nagchowdhuri, P. & Kenney, J. M. (2007). Characterizations of distinct amyloidogenic conformations of the A $\beta$ (1–40) and (1–42) peptides. *Biochem. Biophys. Res. Commun.* **353**, 443–449.
  18. Riek, R., Guntert, P., Dobeli, H., Wipf, B. & Wuthrich, K. (2001). NMR studies in aqueous solution fail to identify significant conformational differences between the monomeric forms of two Alzheimer peptides with widely different plaque-competence, A beta (1–40)(ox) and A beta(1–42)(ox). *Eur. J. Biochem.* **268**, 5930–5936.
  19. Hou, L. M., Shao, H. Y., Zhang, Y. B., Li, H., Menon, N. K., Neuhaus, E. B. *et al.* (2004). Solution NMR studies of the A $\beta$ (1–40) and A $\beta$ (1–42) peptides establish that the Met35 oxidation state affects the mechanism of amyloid formation. *J. Am. Chem. Soc.* **126**, 1992–2005.
  20. Shen, L., Ji, H. F. & Zhang, H. Y. (2008). Why is the C-terminus of A $\beta$ (1–42) more unfolded than that of A $\beta$ (1–40)? Clues from hydrophobic interaction. *J. Phys. Chem. B*, **112**, 3164–3167.
  21. Sgourakis, N. G., Yan, Y. L., McCallum, S. A., Wang, C. Y. & Garcia, A. E. (2007). The Alzheimer's peptides A $\beta$  40 and 42 adopt distinct conformations in water: a combined MD/NMR study. *J. Mol. Biol.* **368**, 1448–1457.
  22. Fradinger, E. A., Monien, B. H., Urbanc, B., Lomakin, A., Tan, M., Li, H. *et al.* (2008). C-Terminal peptides coassemble into A $\beta$ 42 oligomers and protect neurons against A $\beta$ 42-induced neurotoxicity. *Proc. Natl Acad. Sci. USA*, **105**, 14175–14180.
  23. Swendsen, R. H. & Wang, J. S. (1986). Replica Monte-Carlo simulation of spin-glasses. *Phys. Rev. Lett.* **57**, 2607–2609.
  24. Geyer, C. J. (1991). Markov chain Monte Carlo maximum likelihood. In *Computing Science and Statistics: Proceedings of the 23rd Symposium on the Interface* (Keramidas, E. M., ed), pp. 156–163, Interface Foundation, Fairfax Station, VA.
  25. Hukushima, K. & Nemoto, K. (1996). Exchange Monte Carlo method and application to spin glass simulations. *J. Phys. Soc. Jpn.* **65**, 1604–1608.
  26. Sugita, Y. & Okamoto, Y. (1999). Replica-exchange molecular dynamics method for protein folding. *Chem. Phys. Lett.* **314**, 141–151.
  27. Von Helden, G., Hsu, M. T., Gotts, N. & Bowers, M. T. (1993). Carbon cluster cations with up to 84 atoms—structures, formation mechanism, and reactivity. *J. Phys. Chem.* **97**, 8182–8192.
  28. Clemmer, D. E. & Jarrold, M. F. (1997). Ion mobility measurements and their applications to clusters and biomolecules. *J. Mass Spectrom.* **32**, 577–592.
  29. Daura, X., Gademann, K., Jaun, B., Seebach, D., van Gunsteren, W. F. & Mark, A. E. (1999). Peptide folding: when simulation meets experiment. *Angew. Chem. Int. Ed.* **38**, 236–240.
  30. Kim, W. & Hecht, M. H. (2005). Sequence determinants of enhanced amyloidogenicity of Alzheimer A $\beta$  42 peptide relative to A $\beta$  40. *J. Biol. Chem.* **280**, 35069–35076.
  31. Bitan, G., Vollers, S. S. & Teplow, D. B. (2003). Elucidation of primary structure elements controlling early amyloid  $\beta$ -protein oligomerization. *J. Biol. Chem.* **278**, 34882–34889.
  32. Yang, A. S. & Honig, B. (1995). Free-energy determinants of secondary structure formation: 2. Antiparallel  $\beta$ -sheets. *J. Mol. Biol.* **252**, 366–376.
  33. Ma, B. Y. & Nussinov, R. (2000). Molecular dynamics simulations of a beta-hairpin fragment of protein G: balance between side-chain and backbone forces. *J. Mol. Biol.* **296**, 1091–1104.
  34. Gilson, M. K. & Zhou, H. X. (2007). Calculation of protein–ligand binding affinities. *Annu. Rev. Biophys. Biomol. Struct.* **36**, 21–42.
  35. Zhang, S., Iwata, K., Lachenmann, M. J., Peng, J. W., Li, S., Stimson, E. R. *et al.* (2000). The Alzheimer's peptide A $\beta$  adopts a collapsed coil structure in water. *J. Struct. Biol.* **130**, 130–141.
  36. Baumketner, A. & Shea, J. E. (2007). The structure of the Alzheimer amyloid- $\beta$  10–35 peptide probed through replica-exchange molecular dynamics simulations in explicit solvent. *J. Mol. Biol.* **366**, 275–285.
  37. Murray, M., Krone, M., Bernstein, S. L., Baumketner, A., Condron, M., Lazo, N. *et al.* (2008). The amyloid  $\beta$ -protein: experiment and theory on the 21–30 fragment. *J. Phys. Chem.* Submitted.
  38. Condron, M. M., Monien, B. H. & Bitan, G. (2008). Synthesis and purification of highly hydrophobic peptides derived from the C-terminus of amyloid  $\beta$ -protein. *Open Biotechnol. J.* **2**, 87–93.
  39. Baker, E. S., Gidden, J., Fee, D. P., Kemper, P. R., Anderson, S. E. & Bowers, M. T. (2003). 3-Dimensional structural characterization of cationized polyhedral oligomeric silsesquioxanes (POSS) with styryl and

- phenylethyl capping agents. *Int. J. Mass Spectrom.* **227**, 205–216.
40. Mason, E. A. & McDaniel, E. W. (1988). *Transport Properties of Ions in Gases*. Covely, New York.
  41. Lindahl, E., Hess, B. & van der Spoel, D. (2001). GROMACS 3.0: a package for molecular simulation and trajectory analysis. *J. Mol. Model.* **7**, 306–317.
  42. Cornell, W. D., Cieplak, P., Bayly, C. I., Gould, I. R., Merz, K. M., Ferguson, D. M. *et al.* (1995). A 2nd generation force-field for the simulation of proteins, nucleic-acids, and organic-molecules. *J. Am. Chem. Soc.* **117**, 5179–5197.
  43. Dong, J., Canfield, J. M., Mehta, A. K., Shokes, J. E., Tian, B., Childers, W. S. *et al.* (2007). Engineering metal ion coordination to regulate amyloid fibril assembly and toxicity. *Proc. Natl Acad. Sci. USA*, **104**, 13313–13318.
  44. Kaminski, G. A., Friesner, R. A., Tirado-Rives, J. & Jorgensen, W. L. (2001). Evaluation and reparameterization of the OPLS-AA force field for proteins via comparison with accurate quantum chemical calculations on peptides. *J. Phys. Chem. B*, **105**, 6474–6487.
  45. Sorin, E. J. & Pande, V. S. (2005). Exploring the helix-coil transition via all-atom equilibrium ensemble simulations. *Biophys. J.* **88**, 2472–2493.
  46. Nose, S. (1991). Constant temperature molecular-dynamics methods. *Prog. Theor. Phys. Suppl.* **103**, 1–46.
  47. Hess, B., Bekker, H., Berendsen, H. J. C. & Fraaije, J. (1997). LINCS: a linear constraint solver for molecular simulations. *J. Comput. Chem.* **18**, 1463–1472.
  48. Krone, M. G., Baumketner, A., Bernstein, S. L., Wyttenbach, T., Lazo, N. D., Teplow, D. B. *et al.* (2008). Effects of familial Alzheimer's disease mutations on the folding nucleation of the amyloid  $\beta$ -protein. *J. Mol. Biol.* **381**, 221–228.
  49. Essmann, U., Perera, L., Berkowitz, M. L., Darden, T. A., Lee, H. & Pedersen, L. G. (1995). A smooth particle mesh Ewald method. *J. Chem. Phys.* **103**, 8577–8593.
  50. Frishman, D. & Argos, P. (1995). Knowledge-based protein secondary structure assignment. *Proteins Struct. Funct. Genet.* **23**, 566–579.
  51. Mesleh, M. F., Hunter, J. M., Shvartsburg, A. A., Schatz, G. C. & Jarrold, M. F. (1996). Structural information from ion mobility measurements: effects of the long-range potential. *J. Phys. Chem.* **100**, 16082–16086.
  52. Shvartsburg, A. A. & Jarrold, M. F. (1996). An exact hard-spheres scattering model for the mobilities of polyatomic ions. *Chem. Phys. Lett.* **261**, 86–91.
  53. Okur, A., Wickstrom, L., Layten, M., Geney, R., Song, K., Hornak, V. & Simmerling, C. (2006). Improved efficiency of replica exchange simulations through use of a hybrid explicit/implicit solvation model. *J. Chem. Theory Comput.* **2**, 420–433.